Proc. of the 9th Intl. Conf. of Asian Society for Precision Engg. and Nanotechnology (ASPEN 2022)
15–18 November 2022, Singapore. Edited by Nai Mui Ling Sharon and A. Senthil Kumar
doi://10.3850/978-981-18-6021-8_OR-01-0128

Spatial and geometrical-based microstructure in components fabricated by electron beam powder bed fusion

Pan Wang[1,#], Mui Ling Sharon Nai[1], and Yusaku Maruno[2]

[1]Singapore Institute of Manufacturing Technology, 73 Nanyang Drive, 637662, Singapore
[2]Materials Solution Centre, Hitachi Metals Singapore Pte. Ltd., Singapore 629656
[#]Corresponding authors/Email: wangp@simtech.a-star.edu.sg, TEL:+65-67938957

KEYWORDS:Thermal histories,Ti-6Al-4V, CM247LC, Ti-48Al-2Cr-2Nb intermetallic, Electron beam melting, Additive manufacturing

Metal powder bed fusion additive manufacturing (PBF-AM) has attracted great attention from academics to industries in the recent decade. To accelerate the adoption of PBF-AM, its resultant microstructure at the printed component level must be fully understood so as to have tailorable microstructures that can cater to applications' needs. In this study, the microstructures of printed industrial components of different material systems (such as Ti-6Al-4V, Ti-48Al-2Cr-2Nb intermetallic and CM247LC) are investigated. The complex geometrical components with a wide variety of cross-sections that are fabricated by the electron beam (EB) PBF process achieve near fully dense and no distortion. It is found that the resultant microstructure is highly dependent on its material's type and the thermal histories experienced. For the case with Ti-6Al-4V, a gradual change in α+β microstructure and microhardness at different locations in the impeller is observed, which is attributed to the complex thermal gradient and its intrinsic heat treatment. For the case with Ti-48Al-2Cr-2Nb intermetallic, the observed microstructure changes slightly with different locations regarding the fraction and distribution of the coarse γ phase. The change in microstructure can be linked to the location of the sample and their thermal histories. High temperature caused a loss of Al content, in turn, an increase of α_2 phase. For the case with CM247LC, the texture and grain size vary at different locations in the printed turbine wheel, which are attributed to the cooling speed and thermal gradient difference at different locations. These findings provide an in-depth understanding of the material-process-microstructure relationship in the EB-PBF. More importantly, the findings can be extended to a more broad alloys system, such as (i) these alloys like Ti-6Al-4V, whose microstructures are sensitive to the heat input and heat accumulation during the EB-PBF process, (ii) these alloys with a high content of volatile elements (e.g. Mn, Mg, Al, Pb, Zn), such as in Ti-48Al-2Cr-2Nb alloys, resulted in elemental content difference at different locations as volatile elements evaporate more rapidly at hot locations, (iii) single-phase alloys (e.g. Co-Cr alloys, FCC high entropy alloys) or solid solution strengthening alloys (e.g. Inconel 625), where grain size strengthening and strain strengthening mechanisms dominate. Our findings shed the importance of spatial control of microstructure in the PBF AM processes.

1. Introduction

Metal additive manufacturing (AM) has been gaining increasing interest in the past two decades, as many metallic parts fabricated by AM technologies have been commercialized in the aerospace and biomedical industries, and they also have huge potential in other applications [1, 2]. Electron beam melting, also called electron beam powder bed fusion (EB-PBF), is an important powder-bed metal AM technology that is capable of building metallic parts with complex geometries, using the electron beam to selectively melt over the metallic powder bed via a layer-wise mode based on the computer-aided design (CAD) input [3, 4]. EB-PBF has many advantages over other metal AM techniques, for example, high resolution and accuracy, low porosity, high energy efficiency, fast production rate, no impurity, and so on [5-7].

Ti-6Al-4V, CM247LC, and TiAl intermetallic are important materials for aerospace applications. Therefore, many efforts are carried out to successfully develop optimized AM process to obtain fully dense geometries or understand the resultant microstructure and mechanical properties [8-12]. Nowadays, incorporating metal AM techniques into the manufacturing industry is very interesting. The anisotropy and homogeneity of microstructure and mechanical properties of EB-PBF-built metallic parts have become a significant concern recently [13]. Therefore, the fabricated complex metallic industrial parts need to be further evaluated before qualification for industrial application. Herein, we carried out a systemic study to understand the resultant microstructure of three case studies of the industrial components by using Ti-6Al-4V, CM247LC, and Ti-48Al-2Cr-2Nb intermetallic.

2. Experimental procedures

Three types of pre-alloyed powder, Ti-6Al-4V, CM247LC, and Ti-48Al-2Cr-2Nb, as shown in Figure 1, were used for fabricating the

industrial components by using an Arcam A2X EB-PBF system under an optimized parameter. One centrifugal impeller (Ti-6Al-4V) and two turbine wheels (CM247LC and Ti-48Al-2Cr-2Nb). The fabricated components were sectioned from different locations using electrical discharge machining.

The powder morphology was characterized using Zeiss Ultra Plus field emission scanning electron microscope (SEM) coupled with energy dispersive X-ray spectroscopy (EDS). Detailed microstructure characterization on the sectioned samples from the impeller and turbine wheels was performed using OM and SEM equipped with EDS and electron backscattered diffraction (EBSD).

In view that the presence of large and/or irregular defects may strongly affect the performance of industrial parts, it is critical to examine the distribution of defects using non-destructive testing. X-ray Computed Tomography (XCT), which is non-destructive testing technology for industrial products and components, allows visualization of the physical structures in the interior of an object without physically opening or cutting it. Here, the high energy source (450 KV) was used to scan the whole impeller [14], so as to examine the distortion and internal defects (if any, from size and shape), such as pores, lack of fusion within the impeller, and to quantify the volume fraction of pores. The distortion study of the two turbine wheel samples was performed by using Breuckmann Aicon Smartscan 3D Scanner. The 3D scanning was conducted after the turbine wheel was removed from the build plate and under as-print condition. The scanned images were compared with the design files of the turbine wheel used in EB-PBF printing for the difference in dimension. The evaluation of this comparison was performed by using PolyWorks software.

3. Results and discussion

Fig. 1 shows the morphology of the received virgin powders. All of them are less than 150 micros. It is observed that most of the particles are spherical. However, small satellite particles are seen in the received powder. These satellite particles are formed from the solidifying droplets' collisions caused by the atomization chamber's turbulent flow. In addition to the satellites, the spherical pores corresponding to entrapped gas during the atomization process were revealed by cross-sectioned observation (images not shown here). These entrapped gas pores influence the true density and cause defects in the AM parts, as in previous reports [15]. The powder size distribution, and flowability are good enough for EB-PBF. The measured powder packing capacity at the apparent density was ~50%. The value is similar to that of the powder employed in the EB-PBF process [16], implying that the current powder is applicable for the EB-PBF process. In addition, Ti-6Al-4V and Ti-48Al-2Cr-2Nb are comparable, and they are better than CM247LC for sphericity. With processing optimization, all of the powders have been proven to be able to fabricate complex geometrical components with high density. The fabricated impeller and turbine were shown in Figs. 2 and 3.

As shown in Fig. 2, there are no obvious distortions detected and all the locations did not exhibit any defects from XCT detection. This means that no pore and defect bigger than 80 μm existed in the impeller and the impeller was fully consolidated under the present process parameters, implying very highly dense parts could be produced by the EB-PBF technology. However, typical small spherical pores with an average diameter of ~12 μm were observed occasionally. Regardless of the locations and geometries as marked in Fig 2, it was noted that all the porosities were less than 0.12 vol. %. This is a common phenomenon and is mainly caused by the entrapped argon during the production of gas atomized powder [5].

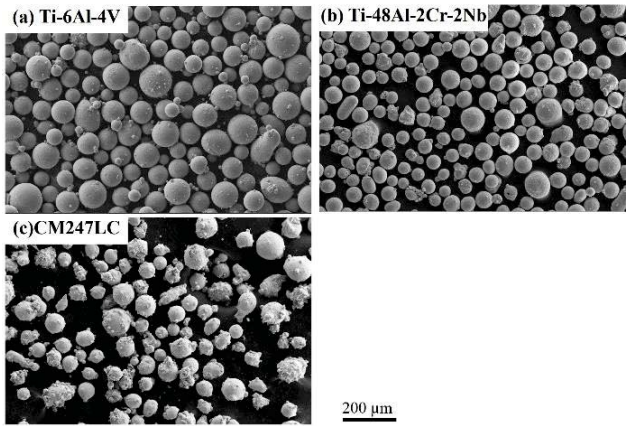

Fig. 1. SEM images of the three powders.

Fig. 2 Picture of EB-PBF-built impeller, its XCT images with sectioned locations, and the polished specimens from different orientations and cut locations, used for microstructure observation, porosity. (a-d) OM images showing the different microstructure and (d') SEM image showing the fine α + β microstructure.

Table 1 Volume fraction of porosity measured from locations in Fig. 2.

A1	A2	A3	B1	B2	B3	C
0.082%	0.067%	0.111%	0.045%	0.089%	0.112%	0.039%

Only α phase and a relatively small fraction of β phase were determined. Fig 2 (a-d) shows the optical microscopy of the sectioned impeller. Although transformed α + β structure, including lamellar colony and basket-weave, were observed in all the observed locations, the size of the α + β microstructure is different. Taking the α lath into consideration (Fig. 2d'), it was observed that the α + β microstructure

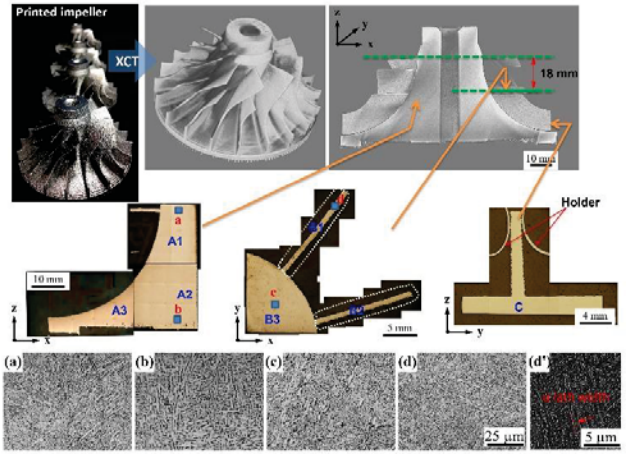

became finer with the increase of build height (Fig. 2 a-b). Within the same build height in X-Y plane, the fine α + β microstructure was observed to coarsen with the increasing cross-sectional thickness (Fig. 2 c-d).

For both turbine wheels using CM247LC and Ti-48Al-2Cr-2Nb, we also obtained a near fully dense part with a density of 99.9% and almost no distortion. We found that the printed part varied between -0.75 to +0.75 mm from the designed part, as shown in Fig. 3. It should be noted that reading in positive values refers to the distortion of bulging out from the part, while negative values refer to distortion of bulging inward into the part. In addition, the EB-PBF-built turbine wheels can be post-processed to meet industrial requirements.

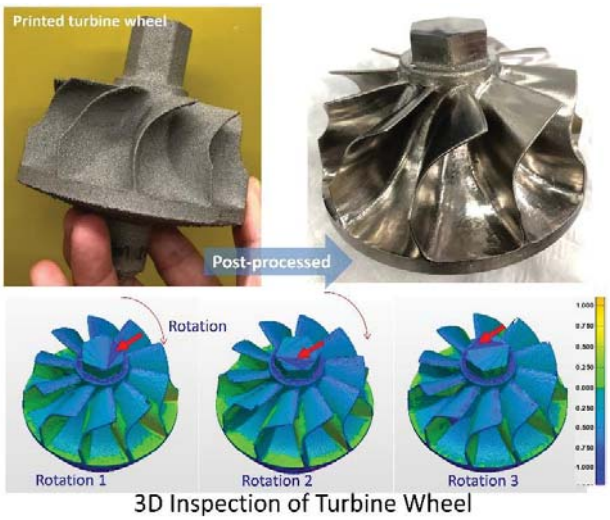

Fig. 3 Picture of EB-PBF-built Ti-48Al-2Cr-2Nb turbine (before and after post-processing) and its 3d inspection results.

Fig. 4 shows the locations for microstructural observation and observed microstructures for Ti-48Al-2Cr-2Nb. The EBSD analysis at five different locations of the turbine wheel revealed that the main phase of EB-PBF Ti-48Al-2Cr-2Nb is γ phase (>99%) and the coarse γ phase band was observed in all the locations. However, the observed microstructure changes slightly with different locations regarding the fraction and distribution of the coarse γ phase. The change in microstructure can be linked to the location of the sample and their thermal histories. It can be seen that location 4 has more heat accumulation than the rest locations. High temperature caused a loss of Al content, in turn, an increase of α_2 phase.

Table 2. Grain size (μm) of samples at different locations from Fig. 4.

	Location 1	Location 2	Location 3	Location 4	Location 5
Average grain diameter	1.91 ± 1.60	1.52 ± 1.35	1.79 ± 1.99	2.29 ± 2.75	2.77 ± 2.09
Excluding band	1.84 ± 1.50	1.52 ± 1.26	1.78 ± 1.65	1.99 ± 1.75	2.62 ±1.77

Table 3. Phase constitution (%) of samples at different locations from Fig. 4.

	Location 1	Location 2	Location 3	Location 4	Location 5
γ	99.71	99.22	98.85	98.14	99.5
α_2	0.23	0.32	1.06	1.68	0.43
Cubic	0.06	0.46	0.09	0.17	0.07

For CM247LC, we observed constant columnar grains in all the locations (Figure 5). However, the width of the columnar grains varied from different locations. As listed in the insert table, location 5 which was at the lowest build height exhibited the largest grain size (138 μm).

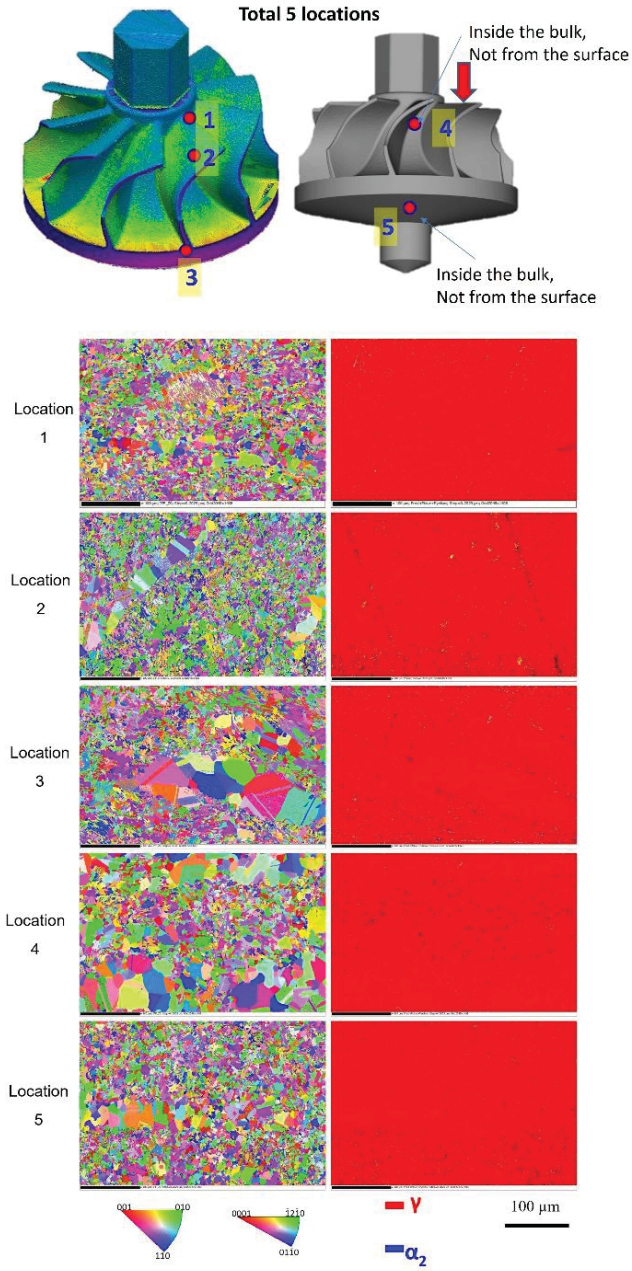

Fig. 4 Sampling locations from turbine wheel (both for Ti-48Al-2Cr-2Nb and CM247LC) and their IPFs and phase maps of all 5 locations (Ti-48Al-2Cr-2Nb).

These changes in microstructure are highly dependent on the materials' phase transformation during the EB-PBF process and their thermal histories experienced. Here we take Ti-6Al-4V impeller as an example to explain how the thermal history influences its final

microstructure. Fig. 6 shows the thermal history at different locations and build height during the EB-PBF process. It is divided into (A) the heating process before melting, (B) the melting of the bottom support structures (named wafer, 10 mm, Fig. 6 a), (C) the melting of the impeller (53 mm, Fig. 6 b-g) and (D) the cooling stage after the completion of the whole process. If the variation of selective melting geometry and area were neglected and each position of the impeller was assumed to undergo a similar thermal history [17], the aging time for the bottom section could be 15 hours longer than that of the top section. The thermal history for bottom, middle and top sections under the above assumption were also illustrated in Fig. 6. Moreover, the cross-section of the impeller gradually decreased with increasing build height (Fig. 6 c-f). This further decreased the thermal input with increasing build height; resulting in the decrease of aging temperature with the increase of build height. It is known that temperature and time are the two critical factors for microstructural coarsening. The longer the aging time and the higher the aging temperature, the coarser the microstructure. Hence, a coarse to fine microstructure could be observed with an increase in build height in the impeller. The fourth possible contribution of the faster cooling rate is the thin blade around the block region. These thin blades with a higher cooling rate acted as a heat transfer path because of the thermal gradient between the blade and block regions. This also increased the cooling rate of the top section that was connected with the blade (Fig. 6 d-f and Fig. 7). The transition section observed in the microhardness provided direct evidence of this heat transfer [18]. The addition of support structures at the bottom section changed the graded microstructure and there is possible to achieve a homogenous

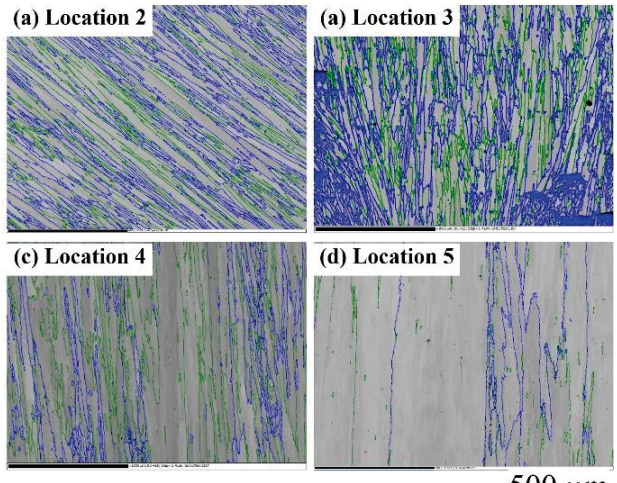

Location 1	Location 2	Location 3	Location 4	Location 5
82	49	34	71	138

microstructure by optimizing the type and length of support structures according to the geometry of the desired component.

Fig. 5 EBSD images showing the columnar grain size change of the CM247LC alloys sectioned from the turbine wheel and the average width of the columnar grains.

4. Conclusions

We have succeeded in fabricating different materials into complex geometrical industrial components with an appropriate process parameter, even for the brittle Ti-48Al-2Cr-2Nb intermetallic in high accuracy with a near fully dense by using EB-PBF technology. However, its resultant microstructure depends on the material types and the locations. This is mainly relevant to the phase transformation behavior during solidification and the thermal history experienced.

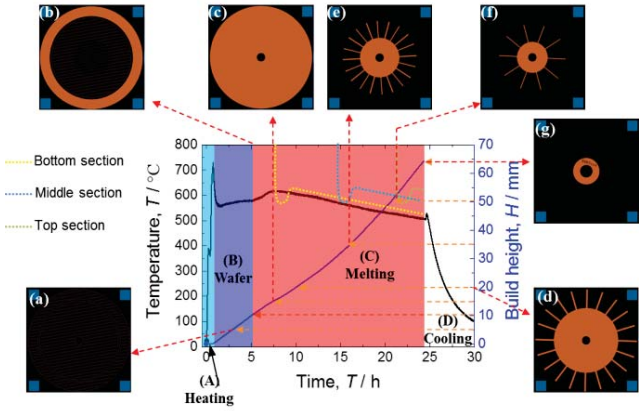

Our findings indicated that the EB-PBF-built microstructure could be predicated on their phase diagram and local thermal histories.

Fig. 6 Temperature (measured by a thermocouple placed beneath the start plate) and build height dependence of build time during the

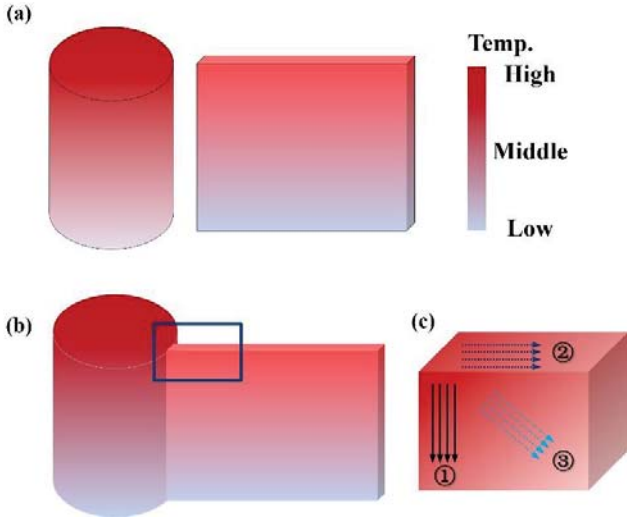

electron beam melting process. (a-g) Geometry variation with the increase of build height.

Fig. 7 Schematic illustration of heat transfer at the transition region between the blade and block. (a) The temperature distribution for the thick block region and thin blade region were built separately. (b) The temperature distribution for the thick block region and thin blade region that were built together. (c) enlarge of the blue square in (b) shows the transition region. There are three types of heat transfer along each temperature gradient.

ACKNOWLEDGEMENT

The Hitachi-SIMTech joint lab and A*STAR Industrial Additive Manufacturing Program: Work Package 3 (Electron Beam Melting)

financially supported the work in the research.

REFERENCES

1. Frazier, W.E., "Metal additive manufacturing: A review", J. Mater. Eng. Perform., Vol.23, No.6, pp. 1917-1928, 2014.
2. Qiu, C., N.J.E. Adkins, H. Hassanin, M.M. Attallah, K. Essa, "In-situ shelling via selective laser melting: Modelling and microstructural characterisation", Mater. Des., Vol.87, No.pp. 845-853, 2015.
3. Wang, P., J. Song, M.L.S. Nai, J. Wei, "Experimental analysis of additively manufactured component and design guidelines for lightweight structures: A case study using electron beam melting", Addi. Manuf., Vol.33, No.pp. 101088, 2020.
4. Mazzoli, A., M. Germani, R. Raffaeli, "Direct fabrication through electron beam melting technology of custom cranial implants designed in a PHANToM-based haptic environment", Mater. Des., Vol.30, No.8, pp. 3186-3192, 2009.
5. Tammas-Williams, S., H. Zhao, F. Léonard, F. Derguti, I. Todd, P. Prangnell, "XCT analysis of the influence of melt strategies on defect population in Ti–6Al–4V components manufactured by Selective Electron Beam Melting", Mater. Charact., Vol.102, No.pp. 47-61, 2015.
6. Al-Bermani, S., M. Blackmore, W. Zhang, I. Todd, "The origin of microstructural diversity, texture, and mechanical properties in electron beam melted Ti-6Al-4V", Metall. Mater. Trans. A, Vol.41, No.13, pp. 3422-3434, 2010.
7. Wang, P., X. Li, S. Luo, M.L.S. Nai, J. Ding, J. Wei, "Additively manufactured heterogeneously porous metallic bone with biostructural functions and bone-like mechanical properties", Journal of Materials Science & Technology, Vol.62, No.pp. 173-179, 2021.
8. Kim, Y.-K., S.-J. Youn, S.-W. Kim, J. Hong, K.-A. Lee, "High-temperature creep behavior of gamma Ti-48Al-2Cr-2Nb alloy additively manufactured by electron beam melting", Mater. Sci. Eng., A, Vol.763, No.pp. 138138, 2019.
9. Todai, M., T. Nakano, T. Liu, H.Y. Yasuda, K. Hagihara, K. Cho, M. Ueda, M. Takeyama, "Effect of building direction on the microstructure and tensile properties of Ti-48Al-2Cr-2Nb alloy additively manufactured by electron beam melting", Addi. Manuf., Vol.13, No.pp. 61-70, 2017.
10. Shanbhag, G., M. Vlasea, "Powder Reuse Cycles in Electron Beam Powder Bed Fusion-Variation of Powder Characteristics", Materials, Vol.14, No.16, pp. 2021.
11. Boswell, J.H., D. Clark, W. Li, M.M. Attallah, "Cracking during thermal post-processing of laser powder bed fabricated CM247LC Ni-superalloy", Mater. Des., Vol.174, No.pp. 107793, 2019.
12. Divya, V.D., R. Muñoz-Moreno, O.M.D.M. Messé, J.S. Barnard, S. Baker, T. Illston, H.J. Stone, "Microstructure of selective laser melted CM247LC nickel-based superalloy and its evolution through heat treatment", Mater. Charact., Vol.114, No.pp. 62-74, 2016.
13. Kok, Y., X.P. Tan, P. Wang, M.L.S. Nai, N.H. Loh, E. Liu, S.B. Tor, "Anisotropy and heterogeneity of microstructure and mechanical properties in metal additive manufacturing: A critical review", Mater. Des., Vol.139, No.pp. 565-586, 2018.
14. MALCOLM, A.A., L. Tong, I.K.B. NG, W.Y. TENG, Y. Tsi Tung, W. Siew Ping, K. Chun Jeng, "A Large Scale Multiple Source X-ray CT System for Aerospace Applications", 5th International Symposium on NDT in Aerospace, No.pp. 2013.
15. Wang, P., P. Huang, F.L. Ng, W.J. Sin, S. Lu, M.L.S. Nai, Z. Dong, J. Wei, "Additively manufactured CoCrFeNiMn high-entropy alloy via pre-alloyed powder", Mater. Des., Vol.168, No.pp. 107576, 2019.
16. Tang, H.P., M. Qian, N. Liu, X.Z. Zhang, G.Y. Yang, J. Wang, "Effect of Powder Reuse Times on Additive Manufacturing of Ti-6Al-4V by Selective Electron Beam Melting", JOM, Vol.67, No.3, pp. 555-563, 2015.
17. Sun, S.-H., Y. Koizumi, S. Kurosu, Y.-P. Li, A. Chiba, "Phase and grain size inhomogeneity and their influences on creep behavior of Co–Cr–Mo alloy additive manufactured by electron beam melting", Acta Mater., Vol.86, No.0, pp. 305-318, 2015.
18. Wang, P., X. Tan, M.L.S. Nai, S.B. Tor, J. Wei, "Spatial and geometrical-based characterization of microstructure and microhardness for an electron beam melted Ti–6Al–4V component", Mater. Des., Vol.95, No.pp. 287-295, 2016.